Numerical Heat Transfer, Part A: Applications Vol. 70, Issue 1, 2016, pp. 14-29
DOI:10.1080/10407782.2016.1139986

Numerical Evidence of an Undisturbed Region of Flow in Turbulent Rectangular Submerged Free Jet

A. Boghi[a], M. Angelino[b], F. Gori[c,*]

[a] Cranfield University, School of Engineering, Environment and Agrifood, Whittle Building, Bld 52, Cranfield, MK43 0AL, UK

[b] Loughborough University, Aeronautical and Automotive Engineering, Stewart Miller Building, Loughborough, Leicestershire, LE11 3TU, UK

[c] University of Rome "Tor Vergata", Via del Politecnico 1, 00133 Roma, Italy

[*] Corresponding author

Keywords: Submerged Rectangular Free Jet; Turbulent Flow; Undisturbed Region of Flow; Numerical Simulation; Large Eddy Simulation, Self-Similarity law.

Abstract

The evolution of turbulent rectangular submerged free jets is described in the literature by the presence of two regions of flow: the potential core region (PCR) and the fully developed region (FDR). However, experiments carried out in the last decade showed that a third region of flow is present, the undisturbed region of flow (URF), so-called in the average visualization, or the negligible disturbances flow (NDF) plus the small disturbances flow (SDF), so-called in the instant visualization. The URF is located between the slot exit and the beginning of the PCR. The main characteristics of URF, and NDF, is that velocity and turbulence profiles remain almost equal to those measured on the slot exit, and the height of the jet remains equal to the slot one. In the SDF the jet height undergoes small variations, contractions or expansions, but without vortex. Up to now, no numerical evidence of the presence of URF has been given by the literature. The present study, which concerns a two-dimensional jet, presents Large Eddy Simulations (LES), carried out at four Reynolds numbers, which are able to predict and characterize URF. The present numerical results are compared to previous theoretical approaches and confirm the presence of URF, between the slot exit and the PCR. Moreover, URF has a self-similar behavior and a new law for the evolution of the momentum is proposed.

1. Introduction

The evolution of turbulent rectangular submerged free jets has been investigated largely in the last decades. Albertson et al. [1] measured the velocity of a jet flow, emerging from a rectangular slot, at several distances from the exit. The structure of the flow was characterized by two-zones: the first one, the closest to the slot exit, was called zone of flow establishment, or near-field region (NFR), and the second one zone of established flow, or fully developed region (FDR), or far-field region. In the NFR the jet mixes with the stagnant fluid at the boundary layer, the velocity on the centerline remains equal to the exit one, and the zone

has been called also potential core region (PCR). The limit of the zone of flow establishment is when mixing has penetrated into the centerline. At the end of PCR a zone of fully developed flow, or fully developed region (FDR), is observed.

The model proposed in [1] confirms the previous theoretical investigations of Tollmien [2] and Görtler [3], about the mixing of homogeneous streams and jet expansions, where the authors proposed different self-similar solutions. These theories have been validated experimentally in several works for the FDR [1, 4-10], and the PCR [11-12].

Even though several experimental observations confirmed the validity of the model proposed in [1], other works showed that, for moderate to small Reynolds numbers and turbulence intensities, there is evidence of a more complex behavior. Brown et al. [13], by studying, with the stroboscopic cinematography, the vortices produced by sound in air jets, observed a column of air, upstream the mixing region, which appears to be undisturbed by the flow. Beavers and Wilson [14] reported the presence of an undisturbed region of flow, while studying the growth of vortices, in the vortex sheets bounding a submerged jet. Chambers et al. [15], using Schlieren photography and spectral coherence measurements, observed an undisturbed region of flow for some jet inlet conditions.

Gori et al. [16] carried out a series of experiments on a free air jet, emerging from a rectangular channel, by using Hot Wire Anemometer (HWA) and shadowgraph visualizations. A region of flow, just outside the exit, where velocity and turbulence remain almost equal to those measured on the slot exit, was observed and called Undisturbed Region of Flow (URF). Its presence was confirmed later with Shadowgraph visualizations and Hot Film Anemometer (HFA) measurements [17-20]. Further experiments [21], conducted with Particle Image Velocimetry (PIV), have recently confirmed the presence of the URF in the average flow. Experiments of the instant flow evolution [22] have shown that the URF can be further divided into two new types of flow, the flow with Negligible Disturbances (NDF) and the flow with Small Disturbances (SDF). In the NDF the jet height remains almost constant, as well as velocity and turbulence profiles, while in the SDF the jet height evidences small variations, either contractions or expansions, but without vortex formation. The experiments have also shown that the length of the URF, equal to the total length of NDF plus SDF, increases with the decrease of Reynolds number.

The URF has not been investigated numerically so far, except in [23], where some preliminary numerical solutions, obtained with the RANS modeling, compared the experimental shadowgraph visualizations at Re=25,000 and 60,000. The numerical analysis can give further information, besides the experiments, which can contribute to a better understanding of the phenomenon of heat transfer upon a cylinder, due to jet flow [24]. This problem has been shown to depend on several variables, as the presence of multiple cylinders in a row [25-26], fins [27], level of turbulence in the jet [28], slot to cylinder diameter ratios [29-30].

The assumption of two-dimensional flow in turbulent conditions has been theoretically justified for some decades with applications to: heat transfer [31], pulsed jet [32], offset jet flow [33], jet flow of nanofluid in a

converging duct [34], meteorology and magneto-hydrodynamics [35]. Some two-dimensional Direct Numerical Simulations (DNS) [36-37] and Large Eddy Simulations (LES) [38-43] have been conducted to study the fluid dynamics of submerged jets, but in none of them the URF has been observed. The advantages of the two-dimensional simulation are the relative rapidity of solution, along with the ability to capture the natural evolution of the structures in the NFR of turbulent jets. Despite the 2D modeling precludes the vortex stretching mechanism, it makes the LES calculations affordable. In addition, the near-field transitional mixing in turbulent jets is dominated by two-dimensional, large-scale coherent structures [44], which are captured in the simulations.

The aim of this paper is to perform a set of numerical simulations, at several Reynolds numbers, in order to establish whether the URF is present between the slot exit and the PCR, like in the experiment of Gori et al. [16-22], or the PCR begins right downstream the slot exit, like in Albertson [1].

2. Numerical Method

2.1 Governing Equations

The Large Eddy Simulation (LES) solves the large-scale turbulent structure at an affordable computational cost, in comparison with the Direct Numerical Simulation, DNS, and models small-scales by spatially filtering the Navier-Stokes equations. Let us define a generic field, $a\left(t,x_i\right)$, function of time t, and a spatial coordinate x_i. The corresponding grid-scale filtered field, $\tilde{a}\left(t,x_i\right)$, is defined by the following integral

$$\tilde{a}\left(t,x_i\right)=\int_{\Omega} a\left(t,\xi_i\right) g\left(x_i-\xi_i,\Delta\right) d^3\xi_i \tag{1}$$

where Ω is the domain dimension, g is a properly normalized spatial filter function, with a characteristic filter width Δ. The effect of the small-scales is embedded in the non-linear terms. For sake of generality the variable will be expressed in a non-dimensional form. The governing equations are:

Continuity equation

$$\frac{\partial \tilde{u}_i}{\partial x_i}=0 \tag{2}$$

Momentum equation

$$\frac{\partial \tilde{u}_i}{\partial t}+\frac{\partial}{\partial x_j}\left(\tilde{u}_i\tilde{u}_j+\tilde{p}\delta_{ij}-\frac{2}{\mathrm{Re}}\tilde{S}_{ij}\right)=\frac{\partial \tau_{ij}^{sgs}}{\partial x_j} \tag{3}$$

where u_i is the velocity vector, p the static pressure, δ_{ij} the identity tensor, Re the Reynolds number, defined as

$$\mathrm{Re} = \frac{U_{in} D_h}{\nu} \tag{4}$$

being U_{in} the inlet velocity, D_h the hydraulic diameter, ν the fluid kinematic viscosity, S_{ij} the shear rate tensor, defined as

$$\tilde{S}_{ij} = \frac{1}{2}\left(\frac{\partial \tilde{u}_i}{\partial x_j} + \frac{\partial \tilde{u}_j}{\partial x_i} \right) - \frac{1}{3}\frac{\partial \tilde{u}_k}{\partial x_k}\delta_{ij} \tag{5}$$

τ_{ij}^{sgs} the sub-grid stress tensor, defined as

$$\tau_{ij}^{sgs} = 2\nu_{sgs}\tilde{S}_{ij} - \frac{2}{3}k_{sgs}\delta_{ij} \tag{6}$$

and

$$\nu_{sgs} = C_S \Delta^2 \tilde{S} \tag{7}$$

the sub-grid viscosity,

$$k_{sgs} = C_I \Delta^2 \tilde{S}^2 \tag{8}$$

the sub-grid kinetic energy,

$$\tilde{S} = \sqrt{2\tilde{S}_{ij}\tilde{S}_{ij}} \tag{9}$$

the filtered shear rate,

$$\Delta = \sqrt{\Delta_k \Delta_k} \tag{10}$$

the filter width, with Δ_k the box filter width in the k-th direction. The dynamic Smagorinsky model is employed in the present study, and its details are illustrated in [42].

2.2 Computational approach

The simulations are carried out with the pisoFoam finite-volume solver, which solves the Navier-Stokes transient incompressible equations via the PISO algorithm, available in the open-source code OpenFOAM. The two-dimensional grid is generated in blockMesh, the OpenFOAM utility for mesh generation. The geometry is made by a rectangular box, three diameters long in the vertical (*y*) direction and 6.5 diameters in

axial (x) direction. The uniform grid is made of 884×408 points with a stencil of 7.3 10^{-3} hydraulic diameters in both directions.

The filter chosen for the LES is the "simple" one, which interpolates the field in a given point with its neighboring cells. The filter amplitude is proportional to the cubic root of the cell volume. A top-hat velocity profile is assumed at the slot exit, in analogy with [1]. The thickness of the shear layer influences the length of the initial region because the smaller it is the shorter is the initial region, as pointed out in [36]. Therefore, since the top-hat velocity profile has the smallest shear layer thickness possible, if the URF is observed in this case, it is surely observable with another inlet velocity profile as well.

Above and below the slot there is a wall, whose thickness is 0.176 hydraulic diameters, in analogy with the experimental conditions of [16-22]. Everywhere else, in the x and y directions, there is a free boundary. At the outlet, the total pressure is specified, and the velocity boundary condition changes, depending on its direction, in order to avoid continuity errors. If the fluid flows out of the domain a zero gradient condition is imposed for the velocity, otherwise the velocity is obtained from the patch-face normal component of the internal-cell value. The explicit time integration scheme is the second order backwards. A different time step, based on the CFL stability criterion, is used for each simulation, so that the CFL is always equal to 0.5. The simulations are carried out for 140 flow times, being the "flow time" the ratio between the domain length and the axial velocity at the slot. After 10 flow times the steady state is reached and the next 130 flow times are used to average the instantaneous variables, in order to obtain the mean turbulent properties.

3. Results and discussion

In order to visualize the jet, Figure 1 reports the instantaneous vorticity contours, which, in a two-dimensional flow, is just a scalar. In order to better visualize the jet, only the absolute value of the variable is considered and the contours are represented in logarithmic scale. The two-dimensional modeling is sufficient to capture the flow features in the near-field region, in spite of the fact that the vortex-stretching is missing in the FDR.

The evolution of the flow field follows the same scheme at all the Reynolds numbers. After the jet exits from the slot the shear layer starts developing. Right after the slot exit there is a region, whose length changes with the Reynolds number, where no vortex is present. The Kelvin-Helmholtz instability appears in the free shear layer at different positions, depending on the Reynolds number. For higher Reynolds number the roller vortex structures are closer to the slot. This is in agreement with the linear theory on Kelvin-Helmholtz instabilities [45], where a low wave number perturbation is enough to trigger the instabilities in a high Reynolds number flow. The vortical structures appear to be bigger at low Reynolds numbers. The roller vortex structures are anti-symmetrical and travel downstream at the speed of convection velocity. Downstream a certain distance from the beginning of the Kelvin-Helmholtz instability, the roller vortices pair to form bigger roller structures. The merging of the shear layers triggers the asymmetry in the flow. The

perturbation of the fluid, at intermediate wave numbers, results in an energy cascade to lower wave numbers, as in three-dimensions. Therefore, in the two-dimensional simulations small vortices aggregate into larger ones.

Figure 1-a shows, at Re = 5000, that the fluid proceeds undisturbed, and the jet height remains nearly constant, up to $x = 1$, where it becomes slightly narrower. This is the point where the Kelvin-Helmholtz instability appears. The jet undergoes some expansions and contractions up to $x = 1.8$, where the first small pair of counter-rotating vortices appear. From $x = 2$ up to $x = 2.4$, the vortices have a cat's eye-shape because of the higher vorticity close to the slot exit, while downstream, where vorticity is smaller, the vortices are round and symmetric. At this Reynolds number, the jet appears mainly symmetric, despite the presence of some asymmetric filaments, expelled from the last couple of vortices.

The vorticity contours at Re = 10,000, Figure 1-b, show a more complex pattern compared to Re = 5000. The undisturbed region of flow, URF, is shorter, ending around $x = 0.8$. The following jet contractions and expansions are smaller in amplitude compared to the previous case. At $x = 1.45$ the first roller vortex pair appears. At each vortex pair corresponds a regular mushroom shaped structure. The jet proceeds up to $x = 2.3$, where, after a considerable contraction, the jet loses its axial structure and becomes a turbulent wake, made of large elliptical vortices with high vorticity, which travel towards the jet axis, and others vortices, which are occasionally expelled and surround it.

Figure 1-c shows the vorticity contours at Re = 20,000. The vortex pairs are smaller and the undisturbed region of flow, URF, is much shorter than in the previous two cases, ending at around $x = 0.15$. Both cat's eye and round vortices are present, forming mushroom structures, up to $x = 2.3$, where the jet becomes asymmetric and vortices of different shapes are expelled from the jet. Closer to the jet the vortices roll faster. When they move away from the centerline the structures slow down and eventually mix with other vortices, expelled afterwards, by forming larger structures with complex shape. At around $x = 3.4$, another mushroom structure, a rounder one, can be seen with larger elliptical eddies. At around $x = 5$, the last mushroom shaped structure is shown.

The vorticity contours at Re = 40,000 are shown in Figure 1-d. In the initial region of flow there are no major differences with the previous case, i.e. Re = 20,000. The undisturbed region of flow, URF, ends at around $x = 0.1$. Then the jet undergoes a series of contractions and expansions, up to around $x = 1$, where they become asymmetric. At around $x = 2$, the jet bends and reaches its smallest section, at around $x = 2.5$, where the flow field loses its axial structure and becomes a turbulent wake. Some mushroom shaped structures, with irregular shape and random orientation, are visible in the wake, as well as elliptical large eddies.

Figure 1 - Instant vorticity contours: (a) Re = 5000; (b) Re = 10,000; (c) Re = 20,000; (d) Re = 40,000.

3.1 Undisturbed region flow (URF)

In the URF the axial velocity changes slightly from the slot exit profile. Therefore, to establish whether an URF is present, in the two-dimensional jet, the axial velocity profile needs to be investigated. The evolution of the axial velocity profiles is studied by analyzing the "isotachs", which are curves with constant velocity in the *x*-*y* plan. This method is particularly useful to identify discontinuity in the flow field. Since in the NFR the average axial velocity profile is symmetric, it is sufficient to consider its evolution only in the upper part of the domain. Because of the top-hat velocity profile on the slot exit, and the no-slip boundary condition at the nozzle wall, all the isotachs are supposed to originate from the point $(x_0,y_0) = (0,h)$, being $h=0.25$ the ratio between the half-length of the slot, $H/2$, and the hydraulic diameter, $2H$.

Figure 2 presents the numerical results of the isotachs for different velocities and Reynolds numbers. The analysis of the isotachs of Figure 2 reveals the presence of a point where the slope of the isotachs changes, being positive for $U \in [0, 0.70]$ and negative for $U \in [0.75, 1]$, regardless of the Reynolds number. The axial length position of the slope change is inversely proportional to the Reynolds number. The slope change indicates that the fluid is subject to different mechanisms, upstream and downstream. The focus of this section of the paper is on the upstream region, between the slot exit and the point of change in slope. For the moment this region is called URF, in analogy to the experiments [16-22], which identifies the first region of flow after the slot exit, and, then, it will be establish if this name is appropriate or not. The fact that the extension of this region is inversely proportional to the Reynolds number seems to give already some credits to the findings of [16-22].

A regression analysis, conducted on the isotachs curves in the URF, allows to find a self-similar law for the URF, with the introduction of a self-similar variable, η, constant along the isotachs, of the following form:

$$\eta = \eta_0 + \sqrt{\mathrm{Re}}\,\frac{(y-h)}{\sqrt{x}} \tag{11}$$

The regression lines are reported in Figure 2, along with the numerical isotachs. The regression lines of the present theory are in very good agreement with the numerical isotachs, up to the point where slope change occurs, for each velocity and Reynolds number. The presence of the constant η_0, in Eq. 11, is necessary in order to explain the fact that the slope of the isotachs is positive for $U \in [0, 0.70]$ and negative for $U \in [0.75, 1]$, regardless of the Reynolds number. Therefore, there must be an isotach curve, in the interval $U \in [0.70, 0.75]$, called critical isotach, which is always parallel to the *x* axis, and independent of the Reynolds number, in the URF.

Figure 2 – Numerical isotachs: *U = 0.1*, black point; *U = 0.4*, circle point; *U = 0.7*, x point; *U = 0.9*, diamond point. Present theory: *U = 0.1*, black line; *U = 0.4*, dot-dashed line; *U = 0.7*, dotted line; *U = 0.9*, dashed line. (a) Re = 5000; (b) Re = 10,000; (c) Re = 20,000; (d) Re = 40,000.

The analysis of the numerical results reveals that turbulence is negligible in the URF, therefore, the instant variables and the mean ones coincide. The analysis of the axial momentum budget shows that in the URF the axial pressure gradient and the axial viscous stresses, along with the local time derivative, are negligible. Then, the axial momentum equation can be reduced to

$$u\frac{\partial u}{\partial x}+v\frac{\partial u}{\partial y}=\frac{1}{\mathrm{Re}}\frac{\partial^2 u}{\partial y^2} \tag{12}$$

The evolution of the axial velocity is dominated by viscous effects, then, the URF cannot be inside the PCR, which has been identified as the region of a jet flow where the fluid can be considered inviscid [1]. Since the axial velocity is function of a self-similar variable, η, and the problem is two-dimensional, the flow can be represented by a stream-function, ψ, defined as

$$\psi=\frac{1}{\sqrt{\mathrm{Re}}}\sqrt{x}\,f(\eta) \tag{13}$$

where $f(\eta)$ is a function of the self-similar variable η, defined by Eq. (11).

The axial-velocity is then self-similar and can be represented by

$$u(\eta)=\frac{\partial\psi}{\partial y}=\frac{df}{d\eta} \tag{14}$$

while the vertical one is not self-similar

$$v(x,\eta)=-\frac{\partial\psi}{\partial x}=-\frac{1}{2}\frac{1}{\sqrt{\mathrm{Re}}}\frac{1}{\sqrt{x}}\left(f-(\eta-\eta_0)\frac{df}{d\eta}\right) \tag{15}$$

Equations (14) and (15) automatically satisfy the continuity equation:

$$\frac{\partial u}{\partial x}+\frac{\partial v}{\partial y}=0 \tag{16}$$

Now, replacing Eqs. (13-15) into Eq. (12), and expressing the spatial derivative as a function of the similarity variable, η, an ordinary differential equation for the function $f(\eta)$, can be obtained

$$\frac{d^3 f}{d\eta^3}+\frac{1}{2}f\frac{d^2 f}{d\eta^2}=0 \tag{17}$$

Equation (17) has been derived by Blasius [46], in order to describe the evolution of the boundary layer in a flat-plate, and by Lessen [47] and Lock [48] to model the laminar free shear layer between two parallel

streams of fluid, with same [47] and different physical properties, [48], but their self-similar variable did not contain the constant η_0.

In order to solve Eq. 17 three boundary conditions are necessary. The first two are:

$$\lim_{\eta \to +\infty} \frac{df(\eta)}{d\eta} = 0 \tag{18}$$

$$\lim_{\eta \to -\infty} \frac{df(\eta)}{d\eta} = 1 \tag{19}$$

In the parallel streams problem, Lessen [47] and Lock [48] imposed a null vertical velocity on the interface between the two streams. This choice cannot be assumed in the present case because the numerical simulations show that the maximum value of the vertical velocity is reached at the interface with the stagnant fluid. In the jet flow inside a stagnant fluid the vertical velocity is null on the centerline, but this condition is difficult to be applied because the similarity variable on the centerline, η, is function of the axial coordinate, *x*, and, by the definition of Eq. (11), η is always largely negative on the centerline. Since the axial velocity profile in the near field region is almost flat, and the interest is to describe the boundary layer, the boundary condition is that the centerline corresponds to $\eta = -\infty$. Therefore, the following condition is assumed

$$\lim_{\eta \to -\infty} f(\eta) = \eta - \eta_0 \tag{20}$$

At this point, the problem is fully determined and the equations can be solved. The third order ordinary differential equation is split into two systems of three first order differential equations, the first one needs to be solved in the range, $-\infty, \eta_0$, and the second one in the range, $\eta_0, +\infty$. The system is solved with the shooting method in order to find the value of the constant η_0. The additional boundary conditions imposed are: the continuity of *f*, $df/d\eta$, and $d^2f/d\eta^2$, at $\eta = \eta_0$.

The solution is obtained with the code MATLAB, through the routine "ode45", which solves the system of non-linear ordinary differential equations with the Runge-Kutta method of fourth order. The results show that $f(\eta_0) = -0.3384$, $df/d\eta|_{\eta_0} = 0.6914$, and $d^2f/d\eta^2|_{\eta_0} = -0.191$ at $\eta = \eta_0 = -0.5288$ (horizontal line), while $f(0) = 0$, $df/d\eta|_0 = 0.5873$, and $d^2f/d\eta^2|_0 = -0.1997$ at $\eta = 0$.

Figure 3 compares the axial velocity profiles, obtained with the present theory, with the numerical results of the simulations, in the URF. The numerical axial velocity profiles are expressed in function of the self-similar variable, $\eta - \eta_0$, and plotted at different axial coordinates, in order to show that the hypothesis of self-similarity is valid. The results, at different Reynolds numbers, show a good agreement, especially at

smaller Reynolds number, because of the wider boundary layer. The velocity profile has an interesting facet, at *y=h*, or $\eta = \eta_0$ (horizontal line), Lock [48] found a value of *0.59* for the parallel streams problem, while the present theory, for a jet flow in stagnant fluid, shows a value of *0.69*, which is in reasonable agreement.

Figure 3 – Numerical axial velocity profiles, at different x distances, and present theory of self-similarity in URF. (a) Re = 5000; (b) Re = 10,000; (c) Re = 20,000; (d) Re = 40,000.

Figure 4 presents the vertical velocity, multiplied by the square root of 4 times the Reynolds number and the axial coordinate, since it is not only function of the self-similar variable, as a function of $\eta - \eta_0$. The numerical vertical velocity profiles, obtained with the LES approach, are reported at different axial coordinates. The theoretical profiles are compared with the numerical results, for the four Reynolds numbers investigated. The vertical velocity approaches zero for η approaching $-\infty$, in agreement with the present theory and differently from Lock [48], where the value reached is *-0.5*. Also, the present theory and the Lock one [48] disagree, in predicting the position of the maximum of the vertical velocity, at $\eta = \eta_0$, which is $0.3378/\sqrt{Re \cdot x}$, in the present theory, while is 0 in the Lock one. This is a further confirmation that, at high Reynolds numbers, the present theory and the Lock one [48] give comparable results and the interface flattens. Moreover, the vertical velocity profile, predicted by the Lock theory [41], varies more inwards the jet than outwards, compared to the present profile, while the two theories converge for $\eta \to +\infty$.

Figures 4-a and 4-b show that the theoretical results lose their agreement with the numerical ones at high values of *x*, because of the difficulty to find the limit of the considered region, URF. Further on, between this region and the next one there is a buffer layer, where the phenomena, dominating in one region, coexist with those in the other one and the transition is fast but not abrupt. At small Reynolds numbers, the numerical results are in better agreement with the present theoretical ones.

Figure 4 - Numerical vertical velocity profiles, at different x distances, and present theory of self-similarity in URF. (a) Re = 5000; (b) Re = 10,000; (c) Re = 20,000; (d) Re = 40,000.

3.2 Potential Core Region (PCR)

The axial velocity profiles are also investigated in the potential core region, PCR, which follows the URF. Figure 5 shows the isotachs curves, obtained with the numerical simulations and already reported in Fig. 2, but a larger span of the abscissa evidences better the two different slopes of each isotach. The region of interest now, PCR, is that with the higher slope.

In the PCR, turbulence is not negligible, therefore, the self-similar analysis must be applied to the mean variables. A suitable variable of self-similarity, η,

$$\eta = \eta_0 + \frac{(y - h_0)}{a(x - x_0)} \tag{21}$$

can represent the axial velocity profiles.

The regression lines, obtained from the present theory, are approximately straight lines with the constant a independent on the Reynolds number, in agreement with the definition of PCR, and they are reported in Figure 5. It is possible to observe the reasonably good agreement between the constant slope of the regression line, and that of each isotach, in the first part of PCR.

Figure 5 – Numerical isotachs: *U = 0.1*, black; *U = 0.4*, circle; *U = 0.7*, x; *U = 0.9*, diamonds. Regression lines: *U = 0.1*, black; *U = 0.4*, dot-dashed; *U = 0.7*, dotted; *U = 0.9*, dashed. (a) Re = 5000; (b) Re = 10,000; (c) Re = 20,000; (d) Re = 40,000.

Tollmien [2] and Görtler [3] proposed a self-similar solution for the velocity profile in the potential core region of a turbulent jet. The self-similar variable is the same of Eq. (21), with the assumption of η_0, h_0, x_0 equal to *0*, and the coefficient a equal to *0.13*, although the experimental values of [21] are around *0.09*, and in Albertson [1], *0.12*.

The analysis of the axial and vertical momentum budget reveals that the equations can be approximated by:

$$U\frac{\partial U}{\partial x} + V\frac{\partial U}{\partial y} = \frac{\partial \tau_{xy}^R}{\partial y} \tag{32}$$

$$0 = -\frac{\partial P}{\partial y} + \frac{\partial \tau_{yy}^R}{\partial y} \tag{23}$$

This result is in agreement with Tollmien [2] and Görtler [3], while the vertical momentum is in agreement with the dimensional analysis of Townsend [49] and the experimental analysis of Miller and Comings [50].

In order to validate the present numerical results, they are compared with the theoretical ones of Tollmien [2] and Görtler [3], by defining:

$$\Psi = a(x - x_0) f(\eta) \tag{24}$$

$$U = \frac{\partial \Psi}{\partial y} = \frac{df}{d\eta} \tag{25}$$

$$V = -\frac{\partial \Psi}{\partial x} = -a\left(f - (\eta - \eta_0)\frac{df}{d\eta} \right) \tag{26}$$

$$\tau_{xy}^{R} = \nu_T \frac{\partial U}{\partial y} \tag{27}$$

At this point the two theories are different, because in Tollmien [2]

$$\nu_T = c^2 \left(x - x_0\right)^2 \left|\frac{\partial U}{\partial y}\right| \tag{28}$$

$$\zeta = \frac{a\left(\eta - \eta_0\right)}{\sqrt[3]{2c^2}} \tag{29}$$

$$\frac{d}{d\zeta}\left(\left|\frac{d^2 f}{d\zeta^2}\right|\frac{d^2 f}{d\zeta^2}\right) + 2 f \frac{d^2 f}{d\zeta^2} = 0 \tag{30}$$

while in Görtler [3]

$$\nu_T = e\left(x - x_0\right) \tag{31}$$

$$\xi = \frac{a^2\left(\eta - \eta_0\right)}{e} \tag{32}$$

$$\frac{d^3 f}{d\xi^3} + f \frac{d^2 f}{d\xi^2} = 0 \tag{33}$$

Equations (30) and (33) are solved by providing the boundary conditions imposed in [2] and [3]. The constants of the model are scaled in such a way that the variables ξ and ζ coincide.

The mean axial velocity profiles, obtained with the present numerical simulations, at different *x* distances, are compared with the Tollmien [2] and Görtler [3] results in Figure 6, as function of $\zeta = \xi$. The numerical results are reported at different axial coordinates, *x*, in order to show that the hypothesis of self-similarity is verified. Both the theories give comparable results at the interface, however, Figure 6 shows that Tollmien [2] results are in better agreement with the numerical data closer to the centerline, while the Görtler [3] ones are better in the outer region. The agreement between the numerical data and the two theories is quite good, even at high Reynolds numbers.

Figure 6 - Numerical axial velocity profiles, at different x distances, and Tollmien (black line) and Görtler (dashed line) theories in PCR. (a) Re = 5000; (b) Re = 10,000; (c) Re = 20,000; (d) Re = 40,000.

Figure 7 compares the theoretical vertical velocity profiles of Tollmien [2] and Görtler [3] with the present numerical results at the four Reynolds numbers, as function of $\zeta = \xi$. The Tollmien [2] theory is in better agreement with the present numerical results in the upper part of the domain, while the Görtler [3] one is in better agreement closer to the centerline. Both theories [2-3] give comparable results at the interface,

where the shape and the position of the maximum are well predicted. The agreement with the numerical results is less satisfactory at high Reynolds numbers.

Figure 7 - Numerical vertical velocity profiles, at different x distances, and Tollmien (black line) and Görtler (dashed line) theories in PCR. (a) Re = 5000; (b) Re = 10,000; (c) Re = 20,000; (d) Re = 40,000.

4. Conclusions

The theoretical approach, employed in the present paper, shows that, in a rectangular submerged free jet, it is possible to identify two self-similar regions of flow. The first one is dominated by the viscous stresses and is identifiable with the undisturbed region of flow, URF, observed in the average flow in [16-21], also described, in the instant flow [22], as negligible disturbances flow, NDF, plus small disturbances flow, SDF. The second region is dominated by turbulence and is identifiable with the potential core region, PCR. According to Albertson [1], when a jet issues from a rectangular slot, a velocity discontinuity is present on the exit of the jet into the surrounding fluid, since its velocity profile may be assumed to be relatively top-hat. The eddies generated in this region of high shear stress result immediately in a lateral mixing process, which progresses both inward and outward with the distance from the exit.

The numerical Large Eddy Simulations, performed in the present paper at four Reynolds numbers, from 5000 to 40,000, show that the eddies are generated only at a certain distance from the slot exit, subdividing the flow-establishment zone, or NFR, into two regions, the first one dominated by the viscous friction and the second one by the turbulent mixing. The first region can be called Undisturbed Region Flow, URF, or Negligible Disturbances Flow, NDF, plus Small Disturbances Flow, SDF, because the velocity profile has slight changes compared to the slot exit, and the jet height varies only slightly. The second region of flow is the well-known Potential Core Region, PCR. The first type of flow, URF, dominated by viscosity, is highly sensitive to the Reynolds number, and seems to disappear around Re = 40,000, where the flow-establishment zone is entirely occupied by the PCR, as in [1].

The results obtained in the present paper confirm, numerically and theoretically, the experimental results discovered in [16-22]. The present two-dimensional approach, comparable to several numerical papers, which considers the near field of the jet flow as an essentially 2D region, is applicable since URF is not affected by turbulence. The solution in the initial, or near field region, is dependent on the top-hat velocity profile imposed on the exit, but, as shown in the literature, this type of velocity profile has a virtually zero shear layer thickness and produces the initial region with the shortest length possible. Therefore, numerical results obtained using a more realistic velocity profile should find an even longer URF.

In conclusion, the present numerical and theoretical results are reliable and confirm that an URF is present in a two-dimensional rectangular submerged jet, as shown experimentally in [16-22]. The results shown suggest that the three-regions flow model for submerged jets, proposed in [16-22] on the basis of the

experimental data, describes better the evolution of the phenomenon, compared with the Albertson model [1].

Acknowledgements

This project has been supported by CINECA/CASPUR with grant number std12-038.

References

[1] M.L. Albertson, Y.B. Dai, R.A. Jensen, and H. Rouse, Diffusion of Submerged Jets, *Transactions of the American Society of Civil Engineers*, 115, 1 (1950): 639–64.

[2] W. Tollmien, Calculation of Turbulent Expansion Processes, *Zeitschrift Für Angewandte Mathematik Und Mechanik*, 6, 6 (1926): 468–78.

[3] H. Görtler, Berechnung von Aufgaben Der Freien Turbulenz Auf Grund Eines Neuen Näherungsansatzes, *Zeitschrift Für Angewandte Mathematik Und Mechanik*, 22, 5 (1942): 244–54.

[4] E. Forthmann, Turbulent jet expansion, *NACA-TM*-7891936.

[5] D.R. Miller, E.W. Comings, Static Pressure Distribution in the Free Turbulent Jet, *Journal of Fluid Mechanics*, 3, 1 (1957): 1–16.

[6] B. G. Van der Hegge Zijnen, Measurements of the Distribution of Heat and Matter in a Plane Turbulent Jet of Air, *Applied Scientific Research*, 7, 4 (1958): 277–92.

[7] L.J.S. Bradbury, The Structure of a Self-Preserving Turbulent Plane Jet, *Journal of Fluid Mechanics*, 23, 1 (1965): 31–64.

[8] E. Gutmark, I. Wygnanski, The Planar Turbulent Jet, *Journal of Fluid Mechanics*, 73, 3 (1976): 465.

[9] A.A. Sfeir, The Velocity and Temperature Fields of Rectangular Jets, *International Journal of Heat and Mass Transfer*, 19, 11 (1976): 1289–97.

[10] A. Krothapalli, D. Baganoff, K. Karamcheti, On the Mixing of a Rectangular Jet, *Journal of Fluid Mechanics*, 107 (1981): 201–210.

[11] H.W. Liepmann, J. Laufer, Investigations of Free Turbulent Mixing, *NACA Technical Note*, 1947.

[12] F.O. Thomas, V.W. Goldschmidt, Structural Characteristics of a Developing Turbulent Planar Jet, *Journal of Fluid Mechanics*, 163 (1986): 227–56.

[13] G.B. Brown, On vortex motion in gaseous jets and the origin of their sensitivity to sound, *Proceedings of the Physical Society*, 47, 703 (1935).

[14] G.S. Beavers, T.A. Wilson, Vortex growth in jets, *Journal of Fluid Mechanics*, 44 (1970): 97–112.

[15] A. Chambers, R. Antonia, L. Browne, Effect of symmetry and asymmetry of turbulent structures on the interaction region of a plane jet, *Experiments in Fluids,* 3 (1985): 343–348.

[16] F. Gori, F. De Nigris, E. Nino, Fluid Dynamics Measurements and Optical Visualization of the Evolution of a Submerged Slot Jet of Air, *The 12th International Heat Transfer Conference, Grenoble, France*, 2 (2002): 303–308.

[17] F. Gori, I. Petracci, Fluid Dynamics Measurements and Numerical Simulations around a Circular Cylinder Impinged by a Submerged Slot Jet of Air, *American Society of Mechanical Engineers, Fluids Engineering Division (Publication) FED*, 259 (2003): 179–185.

[18] F. Gori, I. Petracci, Fluid Dynamics Measurements in a Submerged Free Slot Jet of Air, *14th International Symposium on Transport Phenomena, Bali, Indonesia*, 6–10th July, (2003): 491–496.

[19] F. Gori, E. Nino, Fluid Dynamics Measurements and Flow Visualizations of a Free Slot Jet of Air, *American Society of Mechanical Engineers. Fluids Engineering Division (Publication), FED*, 259, (2003): 187-192.

[20] F. Gori, E. Nino, I. Petracci, Shadowgraph Visualizations of a Submerged Free Slot Jet of Air, *International Journal of Heat and Technology,* 25, 1 (2007): 157–64.

[21] F. Gori, I. Petracci, M. Angelino, Flow Evolution of a Turbulent Submerged Two-Dimensional Rectangular Free Jet of Air. Average Particle Image Velocimetry (PIV) Visualizations and Measurements, *International Journal of Heat and Fluid Flow,* 44, (2013): 764–75.

[22] F. Gori, I. Petracci, M. Angelino, Influence of the Reynolds Number on the Instant Flow Evolution of a Turbulent Rectangular Free Jet of Air, *International Journal of Heat and Fluid Flow*, 50 (2014): 386–401.

[23] F. Gori, M. Angelino, A. Boghi, I. Petracci, Preliminary Numerical Solutions of the Evolution of Free Jets, *ASME International Mechanical Engineering Conference and Exposition, Proceedings (IMECE)*, 7 (D) (2012): 463-469.

[24] F. Gori, I. Petracci, Heat Transfer Measurements and Numerical Simulations in the Cooling of a Circular Cylinder by a Slot Jet of Air, *American Society of Mechanical Engineers, Heat Transfer Division, (Publication) HTD*, 374, 1 (2003): 3-9.

[25] F. Gori, P. Coppa, Circumferential variation of heat transfer on three circular cylinders cooled by a slot jet of air, *International Journal of Heat and Technology*, 16, 2 (1998): 63-69.

[26] F. Gori, I Petracci, V. Tedesco, Cooling of two smooth cylinders in row by a slot jet of air with low turbulence, *Applied Thermal Engineering*, 27, 14-15 (2007) : 2415-2425.

[27] F. Gori, M. Mascia, I. Petracci, Air cooling of a finned cylinder with slot jets of different height, *International Journal of Thermal Sciences,* 50 (2011): 1583-1593.

[28] F. Gori, I. Petracci, Influence of turbulence on heat transfer upon a cylinder impinged by a slot jet of air, *Applied Thermal Engineering*, 49, (2012): 106-117.

[29] F. Gori, I. Petracci, On the Effect of the Slot Height in the Cooling of a Circular Cylinder with a Rectangular Jet, *International Communications in Heat and Mass Transfer*, 48 (2013): 8-14.

[30] F. Gori, I. Petracci, M. Angelino, Experimental and Numerical Heat Transfer on a Cylinder Cooled by Two Rectangular Jets of Different Heights, *ASME International Mechanical Engineering Conference and Exposition, Proceedings (IMECE), Houston, Texas, USA,* 7 (D), (2012): 2679-2688.

[31] P.Y. Tzeng, C.Y. Soong, C.D. Hsieh, Numerical Investigation of Heat Transfer under Confined Impinging Turbulent Slot Jets, *Numerical Heat Transfer, Part A: Applications,* 35, 8 (1999): 903-924.

[32] J. Kechiche, H. Mhiri, G. Le Palec, P. Bournot, Numerical Study of Pulsed Turbulent Plane Wall Jet by Low-Reynolds-Number k–ε Model, *Numerical Heat Transfer, Part A: Applications*, 52, 10 (2007): 935-957.

[33] E. Vishnuvardhanarao, M.K. Das, Computation of Mean Flow and Thermal Characteristics of Incompressible Turbulent Offset Jet Flows, *Numerical Heat Transfer, Part A: Applications*, 53, 8 (2007): 843-869.

[34] M. Rahimi-Esbo, A.A. Ranjbar, A. Ramiar, M. Rahgoshay, A. Arya, Numerical Study of the Turbulent Forced Convection Jet Flow of Nanofluid in a Converging Duct, *Numerical Heat Transfer, Part A: Applications*, 62, 1 (2012): 60-79.

[35] G. Boffetta, R.E. Ecke, Two-Dimensional Turbulence, *Annual Review of Fluid Mechanics,* 44 (2012): 427-451.

[36] S. Stanley, S. Sarkar, Simulations of Spatially Developing Two-Dimensional Shear Layers and Jets, *Theoretical and Computational Fluid Dynamics*, 9, 2 (1997): 121–47.

[37] K. Luo, J. Yan, J. Fan, K. Cen, On Coherent Structures in a Three-Dimensional Transitional Plane Jet, *Science in China Series E: Technological Sciences*, 51, 4 (2008): 386–96.

[38] J. Fan, K. Luo, M.Y. Ha, and K. Cen, Direct numerical simulation of a near-field particle-laden plane turbulent jet, *Physical Review E*, 70, (2004): 026303.

[39] P.E. Des Jardin, S. Frankel, Large eddy simulation of a non-premixed reacting jet: Application and assessment of subgrid-scale combustion models, *Physics of Fluids*, 10, 9 (1998): 2298-2314.

[40] S. James, F.A. Jaberi, Large Scale Simulations of Two-Dimensional Nonpremixed Methane Jet Flames, *Combustion and Flame*, 123, 4 (2000): 465–487.

[41] Y.K. Liu, K.S. Lau, C.K. Chan, Y.C. Guo, W.Y. Lin, Structures of Scalar Transport in 2D Transitional Jet Diffusion Flames by LES, *International Journal of Heat and Mass Transfer,* 46, 20 (2003): 3841–51.

[42] Y. Liu, P.G. Tucker, R.M. Kerr, Linear and nonlinear model large-eddy simulations of a plane jet, *Computers & Fluids*, 37, 4 (May 2008), 439–449.

[43] R. Dutta, B. Srinivasan, A. Dewan, LES of a Turbulent Slot Impinging Jet to Predict Fluid Flow and Heat Transfer, *Numerical Heat Transfer, Part A: Applications*, 64, 10 (2013): 759-776.

[44] M. Lesieur, *Turbulence in Fluids,* 2nd ed. Kluwer Academic, Boston, MA, USA, 1990.

[45] S. Chandrasekhar, *Hydrodynamic and Hydromagnetic Stability*, Clarendon Press, Oxford University Press, 1961.

[46] H. Blasius, Grenzschichten in Flüssigkeiten mit kleiner Reibung, *Z. Math. Phys*. 56 (1908): 1–37.

[47] M. Lessen, On the Stability of the Free Laminar Boundary Layer between Parallel Streams, *N.A.C.A. Tech. Note* 1929, August 1949 (unpublished).

[48] R.C. Lock, The velocity distribution in the laminar boundary layer between parallel streams, *Quart. J. Mech. Appl. Math.,* 4, (1951): 42-63.

[49] A.A. Townsend, *The Structure of Turbulent Shear Flow*, Cambridge University Press, 1956.

[50] D.R. Miller, E.W. Comings, Static Pressure Distribution in the Free Turbulent Jet, *Journal of Fluid Mechanics,* 3, 1 (1957): 1–16.

[51] M. Piller, E. Stalio, Finite-volume compact schemes on staggered grids, *J. Comp. Phys*., 197 (2004): 299–340.

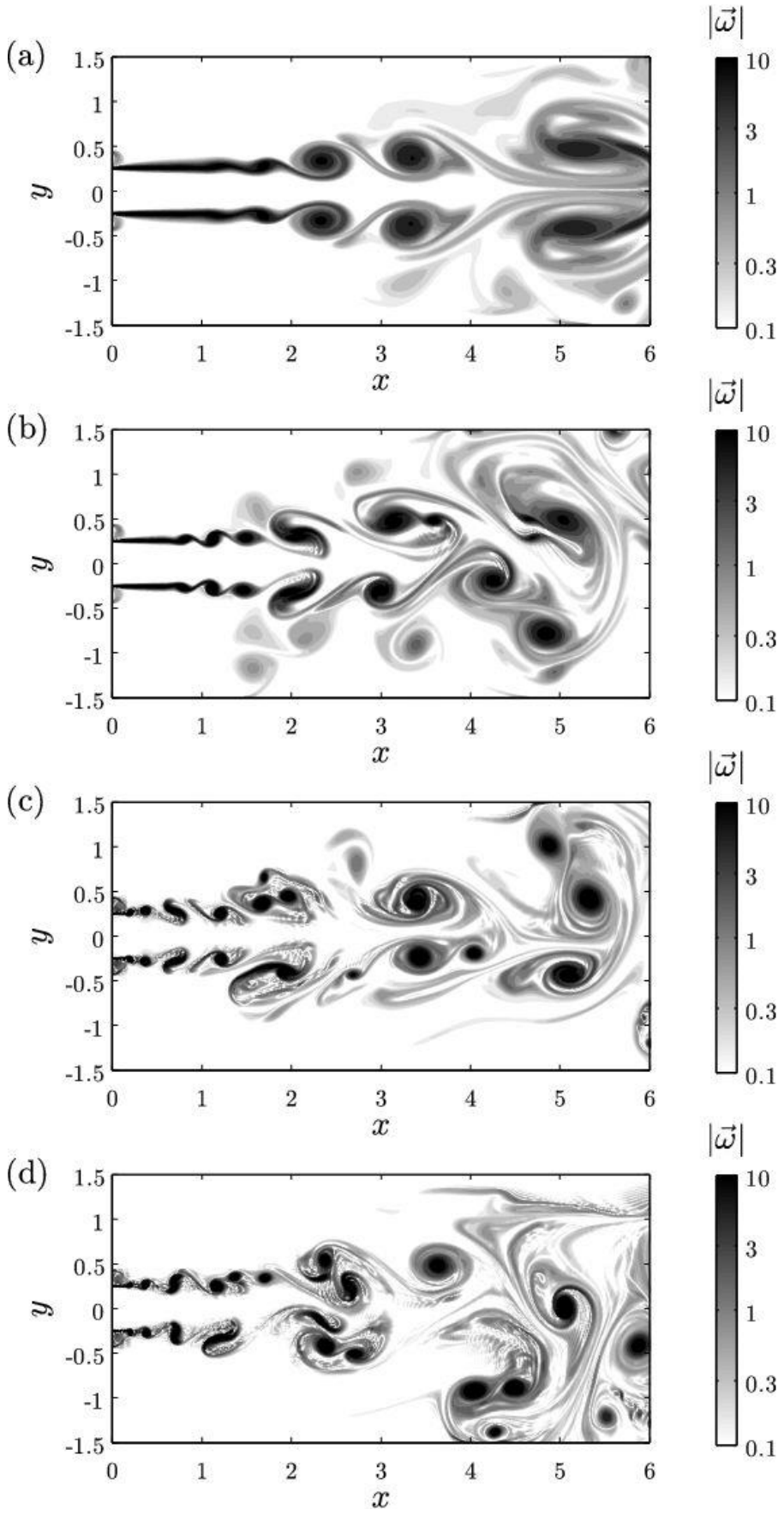

Figure 1 - Instant vorticity contours: (a) Re = 5000; (b) Re = 10,000; (c) Re = 20,000; (d) Re = 40,000.

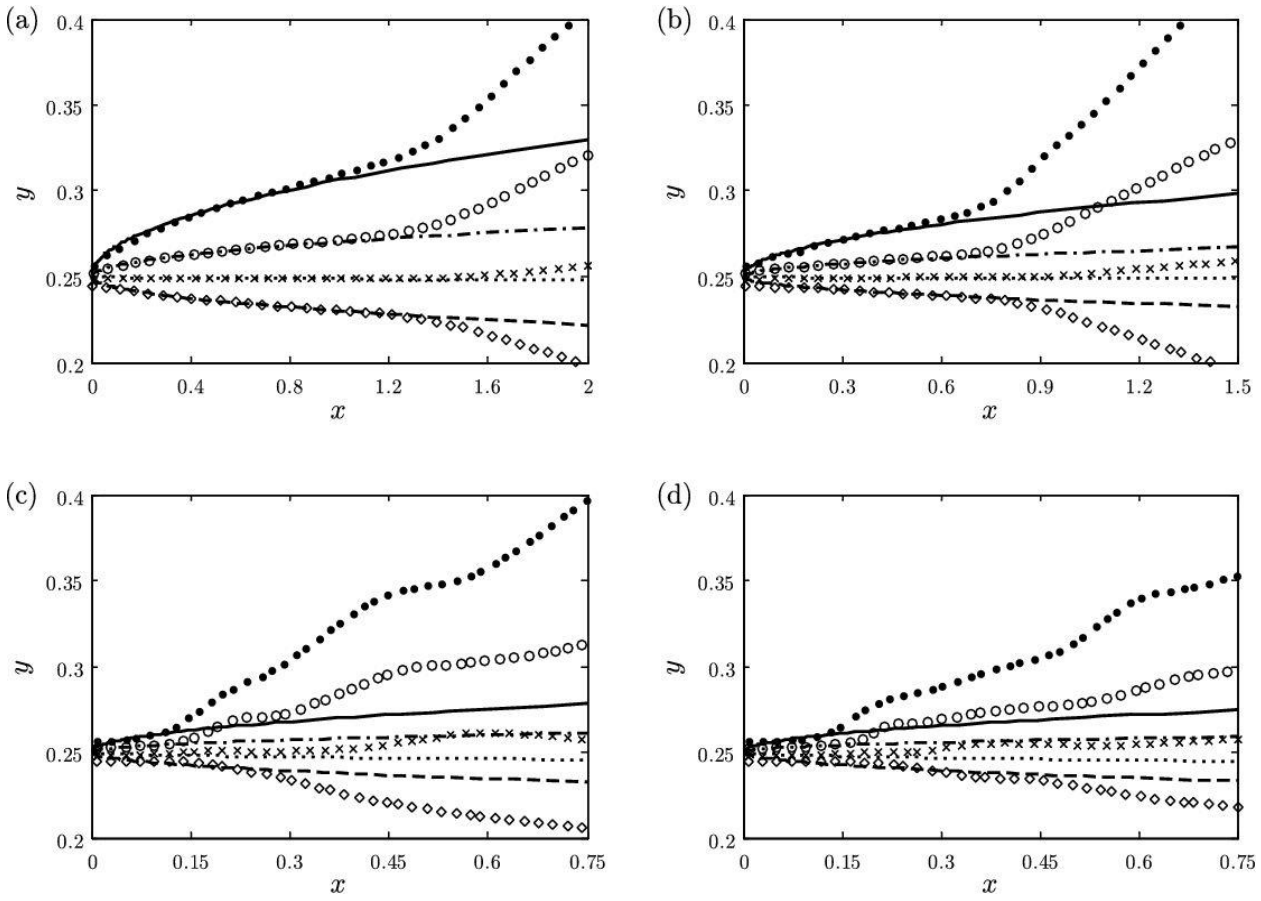

Figure 2 – Numerical isotachs: *U = 0.1*, black point; *U = 0.4*, circle point; *U = 0.7*, x point; *U = 0.9*, diamond point. Present theory: *U = 0.1*, black line; *U = 0.4*, dot-dashed line; *U = 0.7*, dotted line; *U = 0.9*, dashed line. (a) Re = 5000; (b) Re = 10,000; (c) Re = 20,000; (d) Re = 40,000.

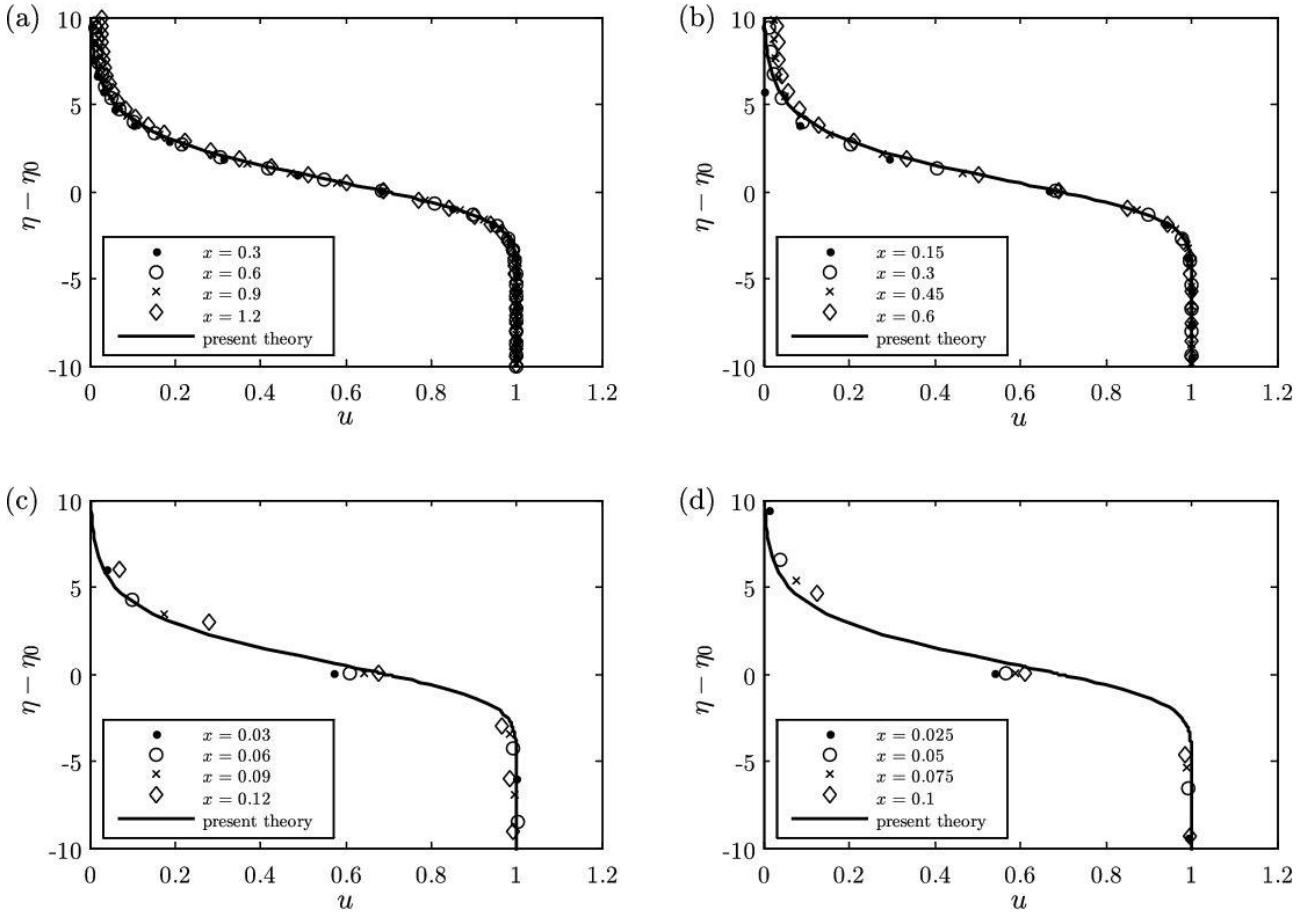

Figure 3 – Numerical axial velocity profiles, at different x distances, and present theory of self-similarity in URF. (a) Re = 5000; (b) Re = 10,000; (c) Re = 20,000; (d) Re = 40,000.

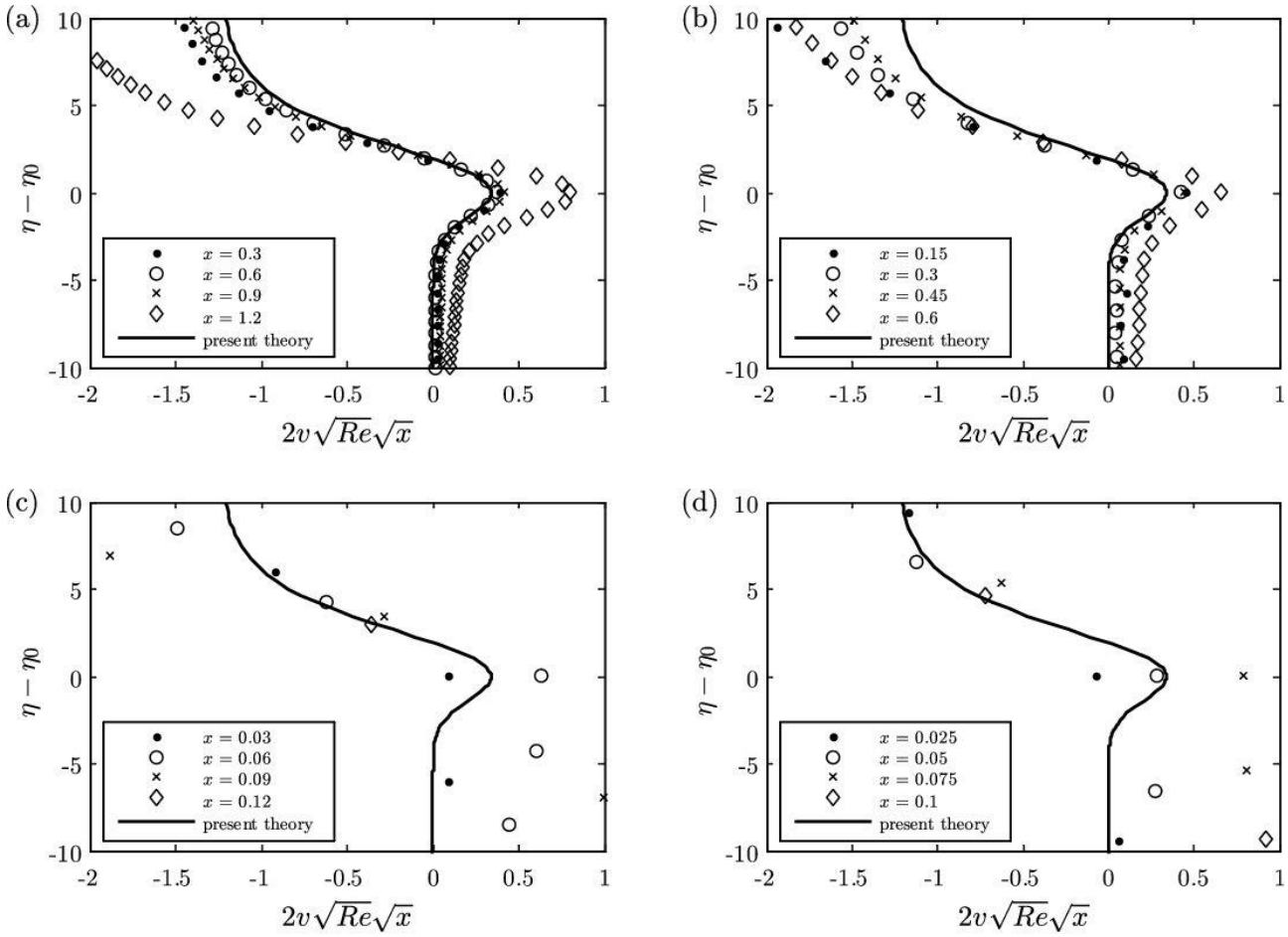

Figure 4 - Numerical vertical velocity profiles, at different x distances, and present theory of self-similarity in URF. (a) Re = 5000; (b) Re = 10,000; (c) Re = 20,000; (d) Re = 40,000.

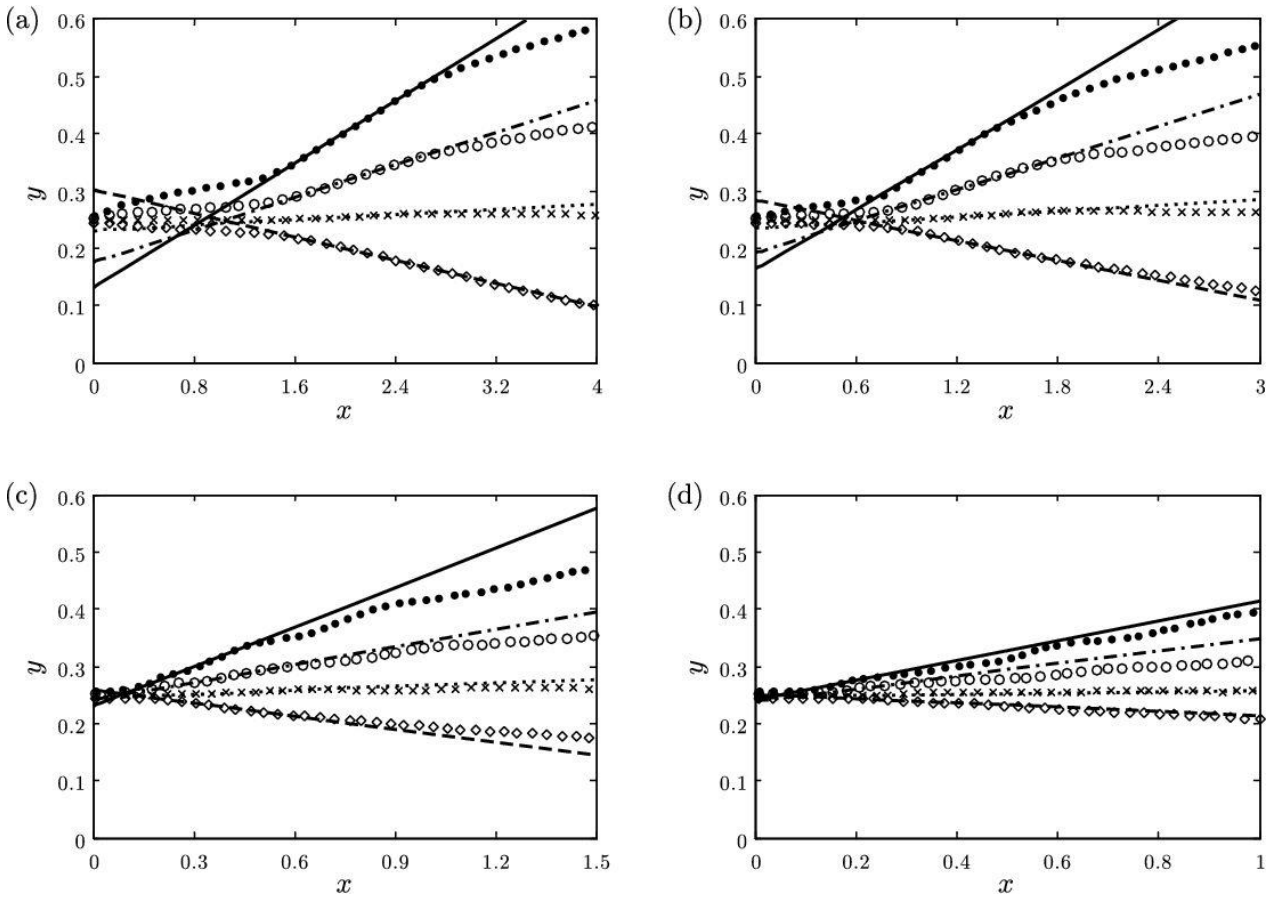

Figure 5 – Numerical isotachs: *U = 0.1*, black; *U = 0.4*, circle; *U = 0.7*, x; *U = 0.9*, diamonds. Regression lines: *U = 0.1*, black; *U = 0.4*, dot-dashed; *U = 0.7*, dotted; *U = 0.9*, dashed. (a) Re = 5000; (b) Re = 10,000; (c) Re = 20,000; (d) Re = 40,000.

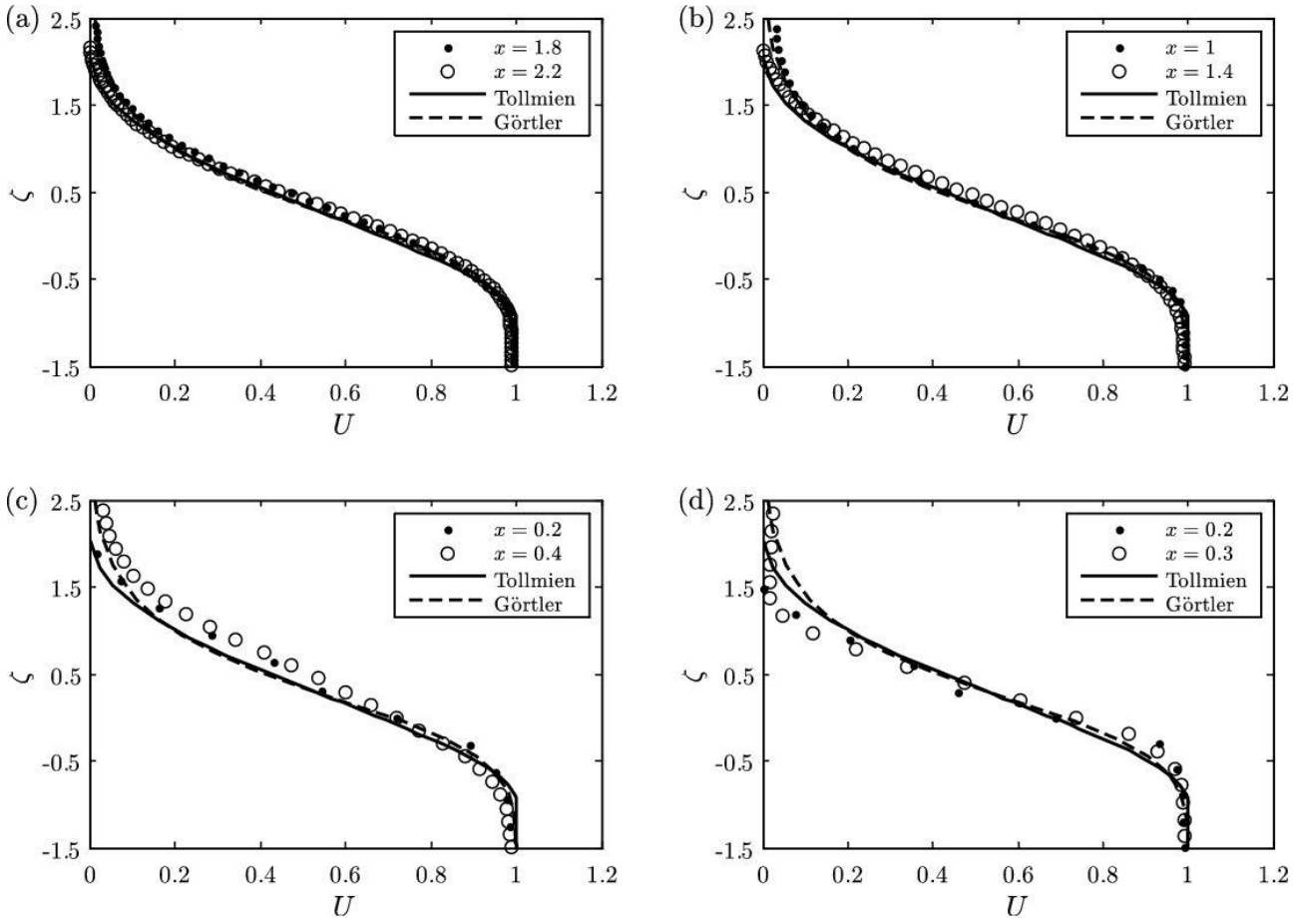

Figure 6 - Numerical axial velocity profiles, at different x distances, and Tollmien (black line) and Görtler (dashed line) theories in PCR. (a) Re = 5000; (b) Re = 10,000; (c) Re = 20,000; (d) Re = 40,000.

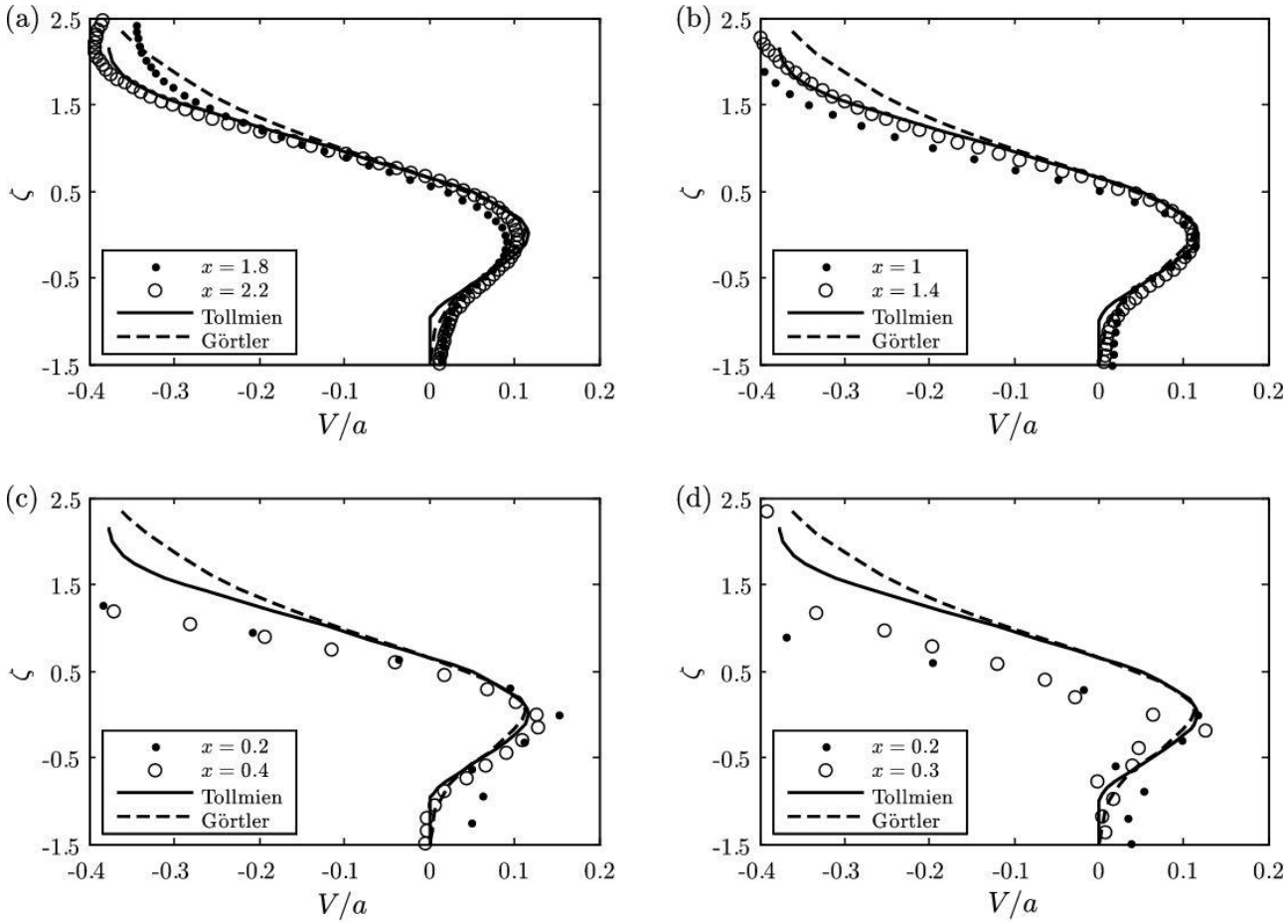

Figure 7 - Numerical vertical velocity profiles, at different x distances, and Tollmien (black line) and Görtler (dashed line) theories in PCR. (a) Re = 5000; (b) Re = 10,000; (c) Re = 20,000; (d) Re = 40,000.